Impact of Green Gold Nanoparticle Coating on Internalization, Trafficking, and Efficiency for Photothermal Therapy of Skin Cancer

Clément Bonamy, Sabrina Pesnel, Maroua Ben Haddada, Olivier Gorgette, Christine Schmitt, Anne-Laure Morel, Nathalie Sauvonnet

ACS OMEGA

http://pubs.acs.org/journal/acsodf

Article

Impact of Green Gold Nanoparticle Coating on Internalization, Trafficking, and Efficiency for Photothermal Therapy of Skin Cancer

Clément Bonamy,[‖] Sabrina Pesnel,[‖] Maroua Ben Haddada, Olivier Gorgette, Christine Schmitt, Anne-Laure Morel,* and Nathalie Sauvonnet*

Cite This: *ACS Omega* 2023, 8, 4092−4105

Read Online

ACCESS | Metrics & More | Article Recommendations | Supporting Information

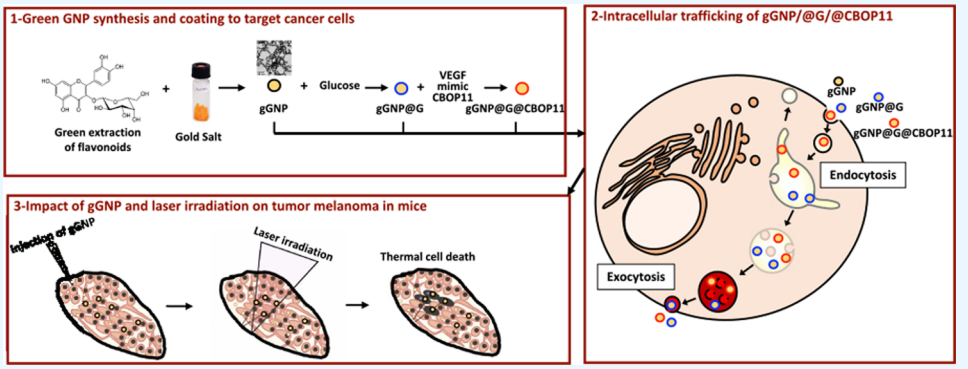

ABSTRACT: Skin cancer is a global health issue and mainly composed of melanoma and nonmelanoma cancers. For the first clinical proof of concept on humans, we decided to study good prognosis skin cancers, i.e., carcinoma basal cell. In UE, the first-line treatment remains surgical resection, healing most of the tumors, but presents aesthetic disadvantages with a high reoccurrence rate on exposed areas. Moreover, the therapeutic indications could extend to melanoma and metastasis, which is a different medical strategy that could combine this treatment. Indeed, patients with late-stage melanoma are in a therapeutic impasse, despite recent targeted and immunological therapies. Photothermal therapy using gold nanoparticles is the subject of many investigations due to their strong potential to treat cancers by physical, thermal destruction. We developed gold nanoparticles synthesized by green chemistry (gGNPs), using endemic plant extract from Reunion Island, which have previously showed their efficiency at a preclinical stage. Here, we demonstrate that these gGNPs are less cytotoxic than gold nanoparticles synthesized by Turkevich's method. Furthermore, our work describes the optimization of gGNP coating and stabilization, also taking into consideration the gGNP path in cells (endocytosis, intracellular trafficking, and exocytosis), their specificity toward cancerous cells, their cytotoxicity, and their in vivo efficiency. Finally, based on the metabolic switch of cancerous cells overexpressing Glut transporters in skin cancers, we demonstrated that glucose-stabilized gGNP (gGNP@G) enables a quick internalization, fourfold higher in cancerous cells in contrast to healthy cells with no side cytotoxicity, which is particularly relevant to target and treat cancer.

INTRODUCTION

Skin cancer is the most common malignancy in the Caucasian population. Its incidence has been increasing over the recent decades, and it is not an artifact of a better screening.[1] General population aging[2] as well as increased recreational UV light exposure could explain this increased incidence.[3] There are two main categories of skin cancers: melanoma and non-melanoma skin cancer, which includes basal cell and squamous cell carcinomas. Malignancies from the latter category are usually not fatal but present high potential of multiple injuries on exposed areas, and the first-line treatment is surgery to remove the tumor. Surgery shows its efficiency to treat these diseases, but according to the size and location of the tumor, it could leave patients disfigured. Melanoma's prognosis is more concerning because it evolves quickly and can spread to other organs. A matter of days/weeks could impact the patient prognosis.[4] Nowadays, 45 years after the first Food and Drug Administration (FDA)-approved drug against metastatic melanoma,[5] the 5-year survival rate to this diagnosis is still below 40%.[6] Therefore, new, innovative therapeutic strategies are needed to improve this prognosis.

Photothermal therapy (PTT) is a treatment based on a nonionizing laser in combination with a light-sensible thermal

Received: November 1, 2022
Accepted: December 29, 2022
Published: January 20, 2023

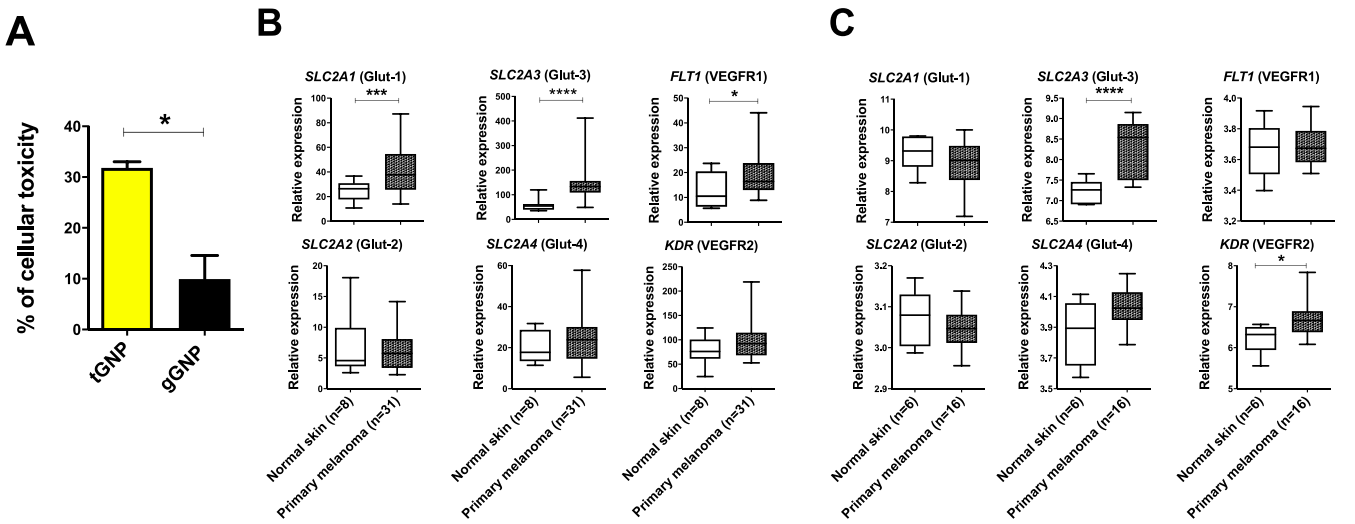

Figure 1. GNP design rational. (A) Comparison of tGNP and gGNP toxicity on healthy human melanocytes (PCS-200-013) using the LDH method and normalized to lysed cells (100%) and control cells (0%). Histograms represent the mean with SEM as error bars. (B,C) Transcription of the *SLC2A1*, *SLC2A2*, *SLC2A3*, *SLC2A4*, *FLT1*, and *KDR* genes coding respectively for Glut-1, Glut-2, Glut-3, Glut-4, VEGFR1, and VEGFR2 proteins in healthy skin and primary melanomas. Box plots are presented on a linear scale for the cohorts of patients GSE46517 (n = 39) (B) and GSE114445 (n = 22) (C). Both cohorts are sourced from historical data sets[49,50] *P < 0,05; ***P < 0,001; ****P < 0,0001 evaluated by the Welch t test.

nanoplatform named photosensitizer. The last decade shows particular interest of PTT in cancer treatment. Recently, Nomura et al. showed that a maintenance of tumor temperature above 43 °C by PTT is enough to cure intradermal tumors in mice.[7] Thanks to their high biocompatibility and surface plasmon resonance (SPR), gold nanoparticles (GNPs) are considered as good photosensitizers when combined with a near-infrared (NIR) laser.[8] Hybrid silica-GNPs are already tested in clinical trials for the treatment of prostate neoplasms.[9,10] Interestingly, treatment of skin lesions, acne vulgaris, using the same hybrid silica-GNPs for PTT shows no side effects, no scars, and a good enough efficiency to be approved by the US FDA.[11]

GNPs are small particles, made of gold, with one of their dimensions in the range of 1 to 100 nm. Their mode of synthesis,[12−14] size,[15−21] shape,[22−25] and coating[26−29] have a great impact on their toxicity,[12−15,22,26] distribution,[16,17] internalization,[17−20,23−25,27−29] and their exocytosis.[21] Our team developed a green, patented protocol to synthesize "green" GNPs (gGNPs).[30,31] Extracts from *Hubertia ambavilla*, an endemic plant from Reunion Island with bioreducing properties, were used to reduce gold salts and to stabilize GNPs. This patented reverse synthesis led to 15 nm spherical gold-core nanoparticles with an average hydrodynamic diameter of 35 to 70 nm, according to the coating, which is considered as an optimal size for endocytosis.[18,32] Previously, we demonstrated the efficiency of PTT, using our gGNPs intratumorally injected, to treat melanoma in mice.[34,35] Since then, we continuously developed our gGNP-candidate to make it the most suitable possible for human use. Particularly, we need gGNPs to stay highly stable in both extracellular and intracellular media. Previous studies from Moros and coworkers reported the interest of a carbohydrate coating in avoiding nonspecific protein and that glucose-coating might increase the intracellular stability of glucose-coated gold nanoparticles.[36−38] In this report, we compared cytotoxicity of gGNP vs the conventional GNP, with same size, but synthesized according to the classical Turkevich's method[39] (tGNP). The study concerned also the functionalized nanoparticles with different coatings: (1) gGNP with no supplemented coating; (2) gGNP@G which is a gGNP stabilized by glucose; and (3) gGNP@G@CBOP11 which is a GNP@G functionalized with CBOP11, a mimic of VEGFR ligand for targeting. We unraveled gGNPs' journey in cells, showed their ability to accumulate in tumor cells, and compared their efficiencies in the treatment of melanoma in mice. It permitted us to select one gGNP-candidate to go into clinical trials.

RESULTS

GNP Synthesis and Coating Design. GNPs were synthesized according two different methods: tGNP was synthesized following Turkevich's protocol using chemicals like citrate,[39] and gGNP was synthesized in a reverse protocol following the green chemistry rules using *Hubertia ambavilla* extracts rich in bioreducer molecules.[30] The macroscopic color change of plant extract/citrate solution after the introduction of the tetrachloroauric acid indicates the expected formation of spherical nanoparticles and was confirmed by UV−visible spectroscopy. An absorption peak was observed around 521 and 537 nm for tGNP and gGNP respectively, which originated from the surface plasmon resonance (SPR) of the gold nanoparticles (Figure S1A,D). The size and shape of the GNPs were further confirmed by measuring the diameter of the Au nanoparticles using the transmission electron microscopy (TEM) images (Figure S1B,E), which indicated that they were predominantly spherical with an average diameter of 15 nm (Figure S1C,F). Since the SPR band position depends on the thickness of the capping molecule shell, we obtained different SPR positions for the same gold core size.[40] To confirm the capacity of these gGNP to be used for PTT, an in vitro study was performed to measure the hyperthermia induced by laser irradiation. A temperature increase of 14 and 20 °C was observed for an irradiation of 0.2 and 0.6 W/cm^2 respectively (Figure S1G,H).

https://doi.org/10.1021/acsomega.2c07054
ACS Omega 2023, 8, 4092−4105

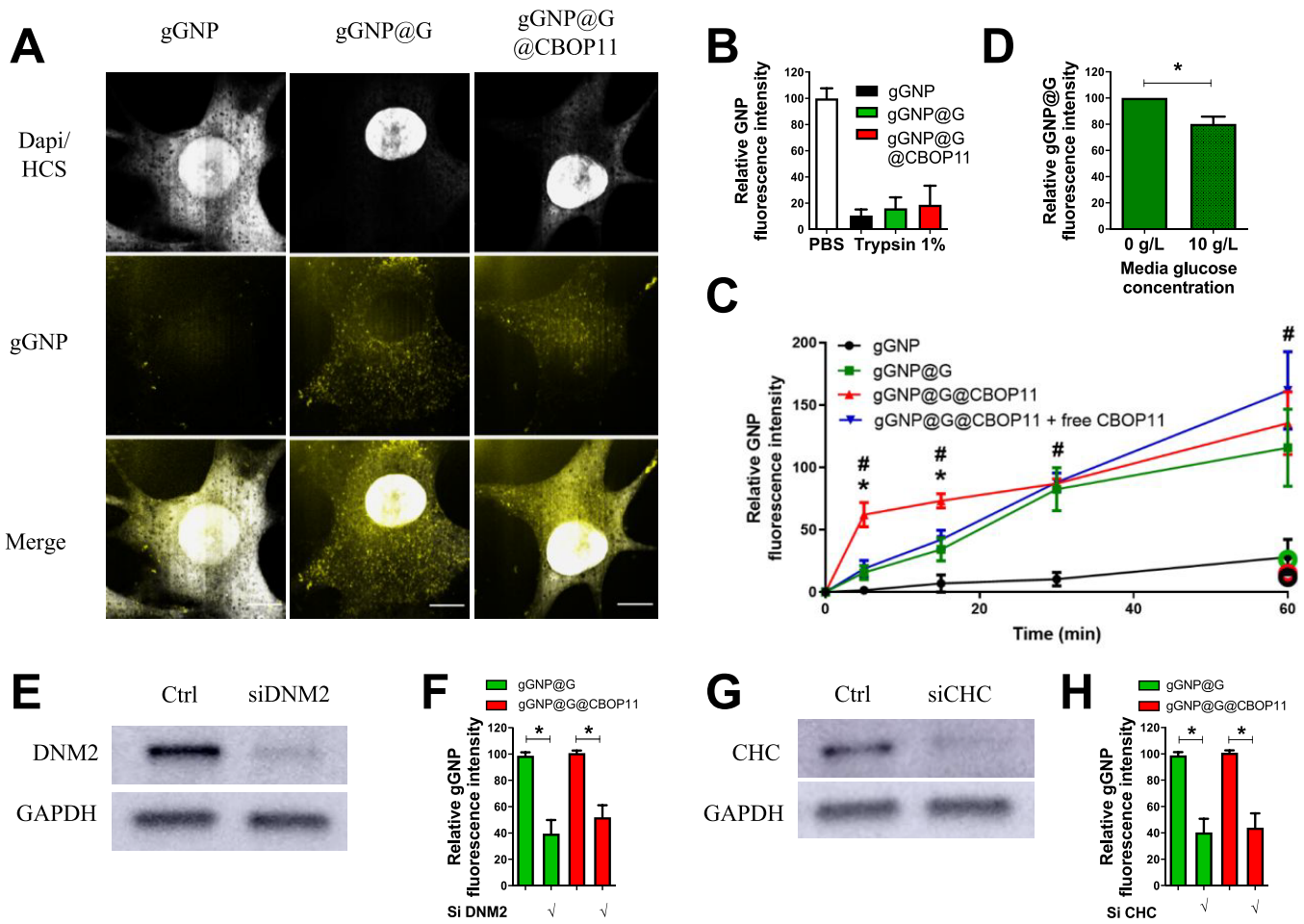

Figure 2. Internalization of gGNP@G and gGNP@G@CBOP11 is an active clathrin/dynamin-dependent process specific of glucose receptors and glucose receptors/VEGFR respectively. (A) Representative images of gGNP (left), gGNP@G (middle), and gGNP@G@CBOP11 (right) internalization in SK-MEL-28. gGNP fluorescence (top), Dapi DAPI and cell marker (HCS) (middle) and merge (bottom) pictures. Cells were incubated for 4 h with gGNP at 6 nM. The scale bar represents 10 μm. (B) Relative fluorescence intensity due to GNPs was assessed by flow cytometry after 1 h incubation of SK-MEL-28 with GNPs at 4 °C. Cells were treated with PBS or trypsin at 1% in order to assess the efficiency of trypsin to detach gGNPs attached to the membrane. (C) Evolution of gGNP (black), gGNP@G (green), and gGNP@G@CBOP11 (red) internalization in the presence or not of free CBOP11 (blue) according to time. Relative fluorescence intensity due to GNPs was assessed by flow cytometry at the different time point. Cells were incubated at 37 °C with gGNPs at 3 nM and then treated with trypsin 1%. Black, green, and red rings represent gGNP, gGNP@G, and gGNP@G@CBOP11 internalization after one hour of incubation at 4 °C, respectively. * Represents the statistical difference with blue and green curves, # with black curve. (D) Relative gGNP fluorescence in SK-MEL-28 cells incubated for 30 min in media with or without glucose containing gGNP@G at 3 nM. Relative fluorescence intensity due to GNPs was assessed by image analysis after observation by a confocal microscope. (E−G) Immunoblotting of cells transfected or not with SiRNAsiRNA against clathrin heavy chain (CHC) (G) or dynamin-2 (DNM2) (E). GAPDH production was assessed as an internal control. (F−H) Relative gGNP fluorescence in SK-MEL-28 cells transfected or not with SiRNAsiRNA against CHC (H) or DNM2 (F) after 30 min incubation with gGNP at 3 nM. Relative fluorescence intensity due to GNPs was assessed by image analysis after observation by a confocal microscope. All experiments were performed at least three times. * or # $P < 0.05$ evaluated by the Welch t test.

We compared cytotoxicity of tGNP and gGNP on healthy melanocytes and on melanoma cells using the lactate dehydrogenase (LDH) secretion. In brief, the LDH release from cells losing their membrane integrity catalyzes the oxidation of pyruvate into lactate and leads to the reduction of NAD+ to NADH that allows the transformation of tetrazolium salt into red formazan quantified by absorbance at 490 nm. In our protocol, supernatants were centrifuged to remove GNPs to avoid background before adding tetrazolium salt. Results are expressed as a percentage of cell death, 100% cell death corresponding to lysed cells and 0% of cell death being the control condition with no GNPs (Figure 1A). After 6 h of incubation, we observed a higher percentage of cell death in cells incubated with tGNP at 6 nM (32%) in comparison with cells incubated with gGNP at the same concentration (10%) in human normal melanocytes (HEMa). Therefore, we further investigated only gGNPs as a nanosensitizer or photoabsorbent agent for the mediation of the plasmonic photothermal destruction. Toxicity of citrate-produced GNPs was already mentioned in the literature.[13,23,29,41−44]

Our goals are to produce highly stable gGNPs in physiological conditions and to specifically accumulate in cancerous cells and optimize their endocytosis in these cells. It is known that in tumors there is (1) a metabolic reprogramming of cells with, notably, an increase of glucose uptake (Warburg effect)[45,46] and (2) an overexpression of VEGFR1/2 at the membrane of cancerous cells inducing an autocrine loop of growth regulation by tumors.[47,48] To confirm

https://doi.org/10.1021/acsomega.2c07054
ACS Omega 2023, 8, 4092−4105

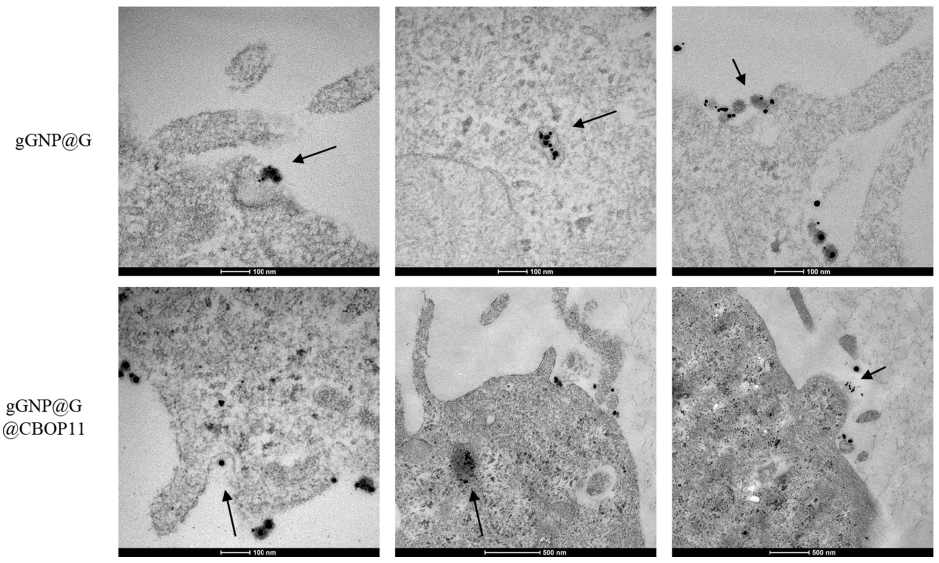

Figure 3. Ultrastructure showing gGNP@G and gGNP@G@CBOP11 journey in SK-MEL-28 cells. Representative TEM pictures of SK-MEL-28 cells incubated for 4 h with 6 nM of gGNP@G or gGNP@G@CBOP11. Arrows show gGNP internalized through pits at the membrane (left), then stored in lysosome-like structure in cells (middle), and finally exocytosed (right).

that glucose transporters, GLUT, and VEGFR1/2 are good cancer markers, we analyzed the expression of GLUT1−4 and VEGFR1/2 encoding genes in tumors of patients with melanoma. We extracted the probe sets for these genes available in two cohorts GSE46517[49] and GSE114445[50] with more than 22 specimens consisting of at least 16 samples of melanomas in a single platform. Levels of GLUT1−4 and VEGFR1/2 gene expression were compared between healthy skin and melanoma specimens. We found that, at least, one GLUT gene −GLUT1 and GLUT3 in GSE46517, GLUT3 in GSE114445− and one VEGFR gene −VEGFR1 in GSE46517 and VEGFR2 in GSE114445− was significantly upregulated in melanomas specimens, compared to healthy skin (Figure 1B,C). The same analysis was performed on cutaneous squamous cell carcinomas, using cohorts GSE32979[51] and GSE53462[52] (Figure S2), and on cutaneous basal cell carcinomas using cohort GSE53462[53] (Figure S3). The same expression pattern was observed: overexpression of GLUT1 and/or GLUT3 and overexpression of VEGFR1 and/or VEGFR2 encoding genes in tumors cells compared to healthy skin. Therefore, we decided to coat our gGNPs with glucose (gGNP@G) to, first, stabilize them and, second, to target GLUT1/3. Then, we developed another gGNP@G candidate also able to target VEGFR1/2 by functionalizing gGNP@G with a VEGF macrocyclic mimic, CBOP11 peptide, gGNP@G@CBOP11.

The stabilization of gGNPs with glucose and their functionalization with CBOP11 peptide were confirmed in our previous study by combining different techniques: Raman spectroscopy, X-ray photoelectron spectroscopy, dynamic light scattering, and zêta potential.[34]

gGNP Internalization Depends on Their Coating. Then, we analyzed the endocytosis of gGNP, gGNP@G, and gGNP@G@CBOP11 in SK-MEL-28, a human melanoma cell line, by immunofluorescence and flow cytometry (Figure 2A−D).

As described in the literature, GNPs could emit fluorescence according to their gold core size.[54] Thus we did not add any fluorescent marker to the gGNP. We observed an efficient uptake of gGNP@G and gGNP@G@CBOP11 in SK-MEL-28 cells in comparison to uncoated gGNPs (Figure 2A). Treatment with trypsin 1% efficiently removed more than 80% of surface-associated gGNP (Figure 2B), thus allowing us to follow the internalization kinetics of gGNPs by flow cytometry (FACS). SK-MEL-28 cells were incubated with different gGNPs from 5 to 60 min, and their internalization was assessed by FACS (Figure 2C). We observed that gGNP@G and gGNP@G@CBOP11 are 8−10 times more internalized than gGNPs after 30 min of incubation. Up to 30 min, the internalization kinetics of gGNP@G@CBOP11 was faster than gGNP@G (Figure 2C). The fact that this difference is not seen later might reflect an equilibrium between endocytosis and intracellular trafficking (recycling and degradation) of nanoparticles mediated by VEGFR. Cells were preincubated with free CBOP11 in order to saturate VEGFR1/2 receptors. We observe a slowdown of the kinetics of gGNP@G@CBOP11 endocytosis, becoming closer to the GNP@G internalization kinetics (Figure 2C). This reveals that CBOP11 could speed up the endocytosis of gGNP@G at early time points. Then, we tested the effect of glucose coupling on gGNP@G internalization by adding glucose for 30 min. Glucose supplementation reduces by 20% gGNP@G internalization (Figure 2D). Altogether, these data indicate that gGNP@G and gGNP@G@CBOP11 are efficiently internalized in a glucose- and glucose/CBOP11-dependent manner, respectively.

Internalization of gGNP@G and gGNP@G@CBOP11 Is an Active, Dynamin-, and Clathrin-Dependent Process. Several endocytosis pathways exist. As GLUT and VEGFR are both internalized by clathrin-dependent or clathrin-independent dynamin-dependent processes,[55−59] we tested if the same pathways were involved in gGNP@G and gGNP@G@CBOP11 internalization. First, we observed that the internalization level of gGNP@G and gGNP@G@CBOP11 is much higher after 1 h of incubation at 37 °C rather than 4 °C, which is not the case for gGNP (Figure 2C), suggesting that only gGNP@G and gGNP@G@CBOP11 are internalized through an active pathway. Then, we depleted either dynamin-2 (DNM2) protein, a pinchase enzyme involved in the fission

https://doi.org/10.1021/acsomega.2c07054
ACS Omega 2023, 8, 4092−4105

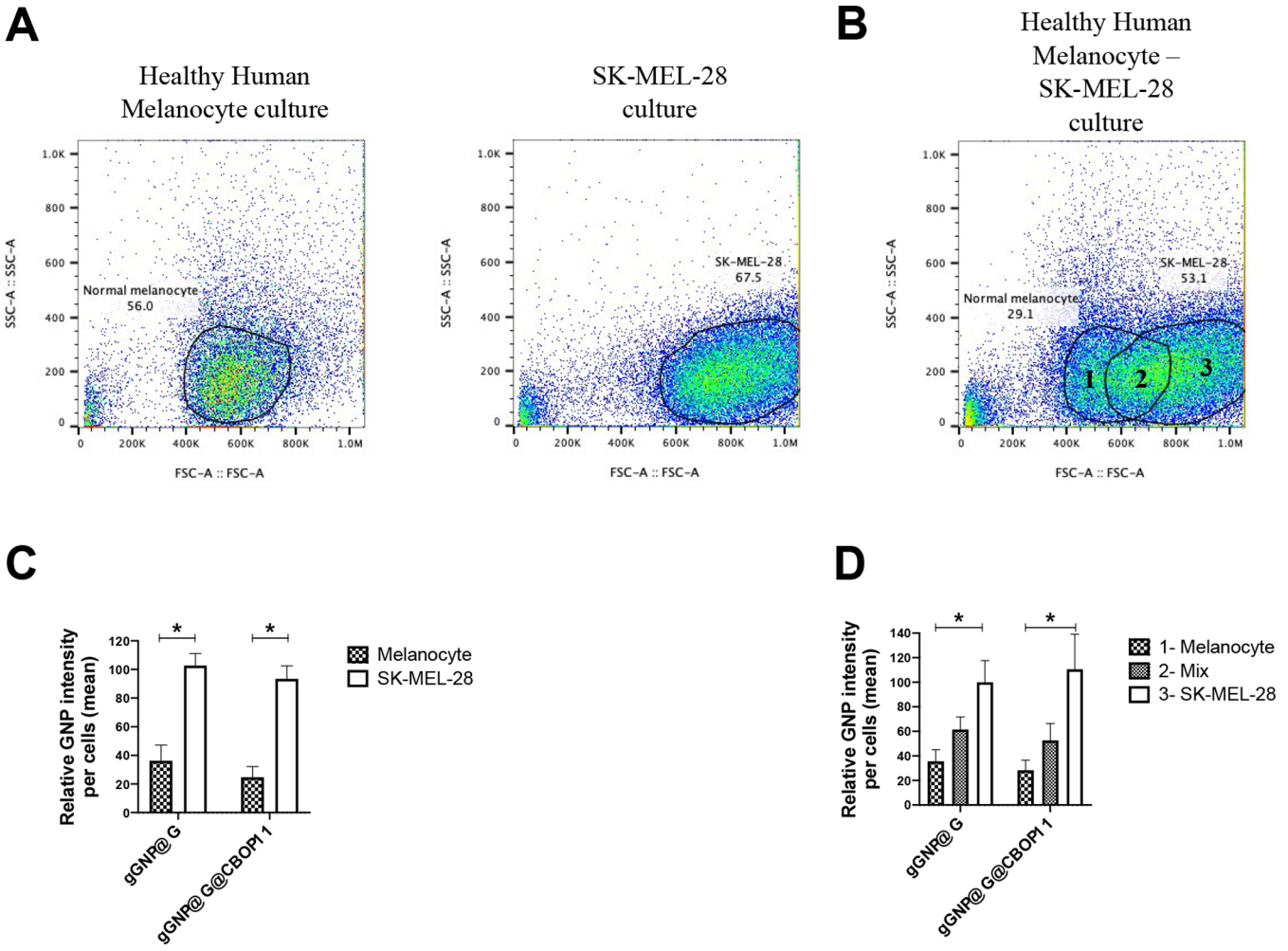

Figure 4. Enhanced gGNP@G and gGNP@G@CBOP11 internalization in cancerous cells. (A,B) Gating strategy of population analyzed in (C) and (D), respectively. (C) Comparison of internalization of gGNP@G and gGNP@G@CBOP11 in SK-MEL-28 or in healthy melanocytes cultivated separately. (D) Comparison of internalization of gGNP@G and gGNP@G@CBOP11 in SK-MEL-28 or in healthy melanocytes cultivated together. "Human Melanocyte" and "SK-MEL-28" populations are composed of a majority of human melanocyte and SK-MEL-28, respectively. The "Mix" population is a population of healthy melanocyte and SK-MEL-28 cells that are not distinguishable through the FSC channel. The proportion of healthy melanocyte/SK-MEL-28 is between the same ratio in "Human Melanocyte" and in "SK-MEL-28" populations. (C,D) Cells were incubated with gGNP@G and gGNP@G@CBOP11 at 6 nM for 30 min. Gold fluorescence intensity was assessed by flow cytometry. *$P < 0.05$ evaluated by the Welch t test.

of endocytic vesicles from the plasma membrane (Figure 2E), or the CHC protein, a coated protein involved in clathrin-dependent endocytosis (Figure 2G), by transfection of specific siRNA. In both cases (Figure 2F−H), we observed a 50−60% decrease of gGNP@G and gGNP@G@CBOP11 internalization when either DNM2 or CHC was depleted. TEM images (Figure 3, left) showed the presence of gGNP@G and gGNP@G@CBOP11 in endocytic pits resembling clathrin-coated ones, confirming that gGNP@G and gGNP@G@CBOP11 are actively internalized by SK-MEL-28 cells in a dynamin- and clathrin-dependent process.

Internalization of gGNP@G and gGNP@G@CBOP11 Is Specifically Enhanced in Cancerous Cells in Comparison with Healthy Cells. The fact that glucose or CBOP11 coupling boosted gGNP@G or gGNP@G@CBOP11 endocytosis indicates that these nanoparticles enter via glut transporters or VEGFR which are both overexpressed in melanomas. Thus, we tested if gGNP@G and gGNP@G@CBOP11 internalizations were higher in malignant cells in contrast to healthy ones by comparing their uptake in SK-MEL-28 cells, derived from a melanoma of a 51-year-old human male, and in normal primary human melanocytes of an adult (HEMa) (ATCC − PCS-200-013). For that, we first incubated cells separately with the gGNPs for 30 min, detached them with trypsin 1%, and analyzed them by FACS (Figure 4C). In both cases, we observed a 3−4-fold gGNP internalization in cancerous SK-MEL-28 cells than in healthy HEMa cells. Then, to better mimic the tumor environment in vitro, we cocultivated the two cell types and segregated these cells by FACS through the FSC channel (Figure 4A). When cocultured, three populations are present: a low FSC one, mainly composed of HEMa cells (1), the second one with high FSC, mainly composed of SK-MEL-28 cells (3), and an intermediate FSC population, composed of both HEMa and SK-MEL-28 cells (2) (Figure 4C). For both gGNPs, we observed an increase gGNP intensity in cells according to the SK-MEL-28/HEMa ratio with also 3−4 times more gGNPs internalized in the SK-MEL-28 population (3) in comparison to gGNPs internalized in the HEMa population (1) (Figure 4D). Therefore, in our model, we showed that gGNP@G and

https://doi.org/10.1021/acsomega.2c07054
ACS Omega 2023, 8, 4092−4105

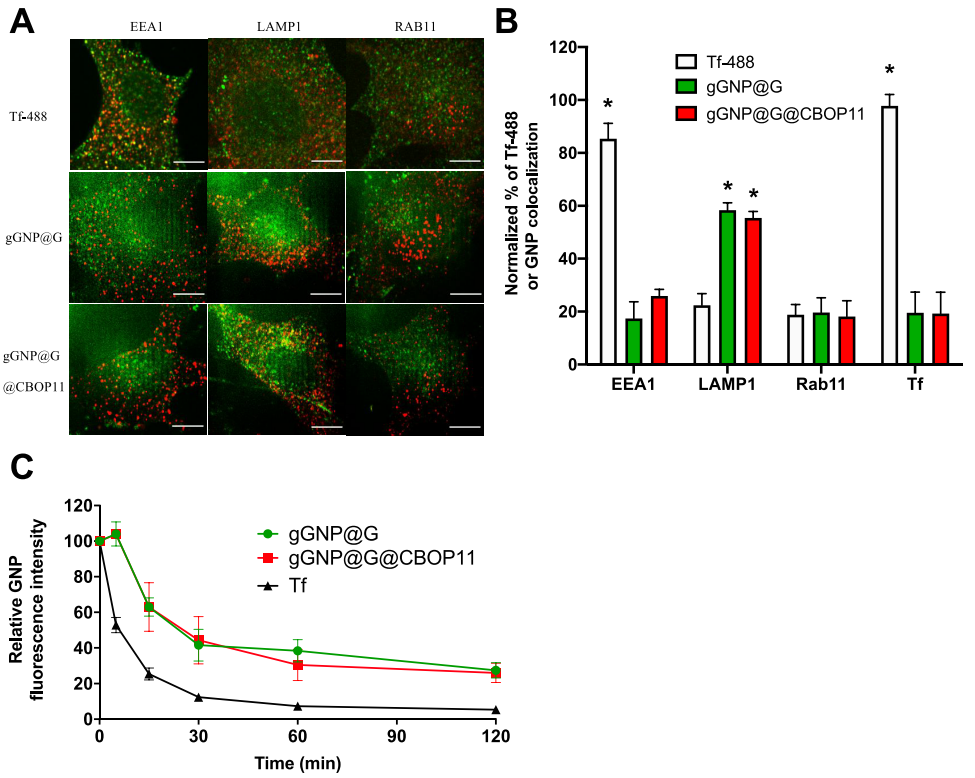

Figure 5. Intracellular trafficking and exocytosis of gGNP@G and gGNP@G@CBOP11 in SK-MEL-28 cells. (A) Representative images of tf-488 (top), gGNP@G (middle), and gGNP@G@CBOP11 (bottom) colocalization with EEA1 (left), LAMP1 (middle), and RAB11 (right) endosomes in SK-MEL-28. Cells were incubated for 4 h with gGNP at 6 nM. The scale bar represents 10 μm. (B) Colocalization ratio of Tf-488 (white), gGNP@G (green), and gGNP@G@CBOP11 (red) with EEA1, LAMP1, and RAB11 endosomes. Colocalization with Tf-647 positive endosomes is used as an internal control. (C) Evolution of transferrin (Tf, blue), gGNP@G (green), and gGNP@G@CBOP11 (red) exocytosis according to time. Relative fluorescence intensity due to gold nanoparticles was assessed by image analysis after observation at a confocal microscope at the different time point. Cells were incubated at 37 °C with gGNP at 3 nM during 4 h, then washed twice, and incubated with media/SVF for different time points. All experiments were performed at least three times. *$P < 0.05$ evaluated by the Welch t test.

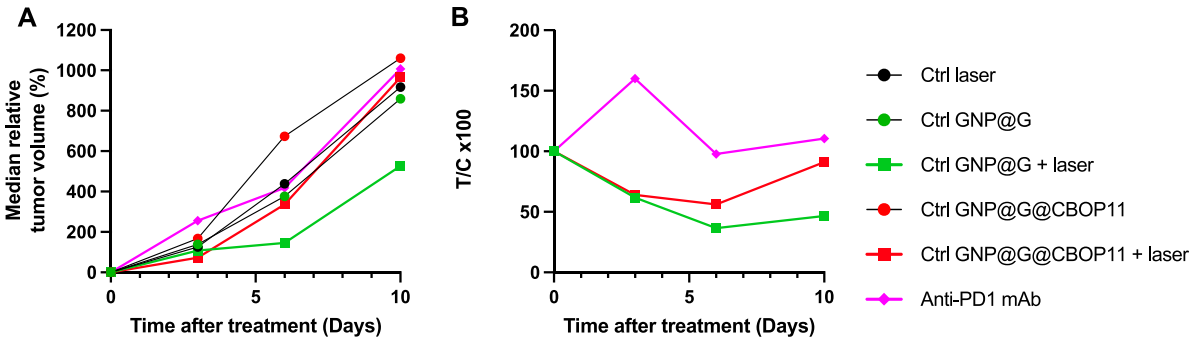

Figure 6. Effect of nanoparticles and laser irradiation on the tumor volume of mice bearing subcutaneous B16F10 murine melanoma xenograft. Evolution of median relative tumor volume (A) or T/C ratio (B) after treatment with 0.3 mg/mL GNP@G (±laser at 0.2 W/cm^2), 0.3 mg/mL GNP@G@CBOP11 (±laser at 0.2 W/cm^2), laser at 0.2 W/cm^2 only, or 5 mg/kg every 5 days of anti-PD1 mAb. Five mice per condition were included.

gGNP@G@CBOP11 are specifically more internalized in cancerous cells than in healthy cells.

Intracellular Trafficking and Exocytosis of gGNP@G and gGNP@G@CBOP11 in Tumor Cells. To better understand the fate of internalized gGNP in cells, we studied intracellular trafficking and putative exocytosis of gGNP@G and gGNP@G@CBOP11 in SK-MEL-28 cells. First, cells were incubated for 4 h with gGNP@G, gGNP@G@CBOP11, or fluorescent transferrin as a control. After fixation, EEA1 (marker of early endosomes), LAMP1 (marker of lysosomes), or RAB11 (marker of recycling endosomes) compartment was stained, and the colocalization ratio was calculated and normalized to have 100% colocalization of Tf-488 positive compartments with Tf-647 positive compartments (Figure 5A,B). Both gGNP@G and gGNP@G@CBOP11 show the same intracellular trafficking with 50−60% of colocalization with LAMP1 positive compartments suggesting that gGNPs are sorted toward lysosomes. TEM images confirmed that gGNP@G and gGNP@G@CBOP11 can be located in lysosomal-like structures (Figure 3, middle).

Then we studied gGNP exocytosis, by incubating SK-MEL-28 cells with Tf-AF647 and gGNP@G or gGNP@G@

https://doi.org/10.1021/acsomega.2c07054
ACS Omega 2023, 8, 4092−4105

Table 1. Antitumor Activity of gGNP@G and gGNP@G@CBOP11 Compared to Reference Treatment against the Subcutaneous B16F10 Murine Melanoma Xenografts

			inhibition of tumor growth		
compound	dose	administration route	rAUC[a]	optimal T/C[b] (%)	activity rating[c]
gGNP@G	0.3 mg/mL	i.t.	55	36.6	L
gGNP@G@CBOP11	0.3 mg/m	i.t.	67	56.0	L
anti-PD1 mAb	5 mg/kg	i.p.	113	97.8	0

[a]rAUC = relative area under the tumor growth curve (expressed as a percentage of the median area under the tumor growth curve of the control group). [b]T/C = (median tumor volume of drug-treated group/median tumor volume of control group) × 100; according to NCI criteria, a T/C ≤ 42% is the minimum level for activity.[33] The optimal T/C is the lowest value, reflecting the maximal tumor growth inhibition. [c]Activity Rating: "0": inactivity if T/C > 42%; "L": low level of activity if T/C ≤ 42%; "H": High level of activity if T/C ≤ 10%; "T": toxicity if body weight loss >20% or % presumed drug-related death >20%.[33]

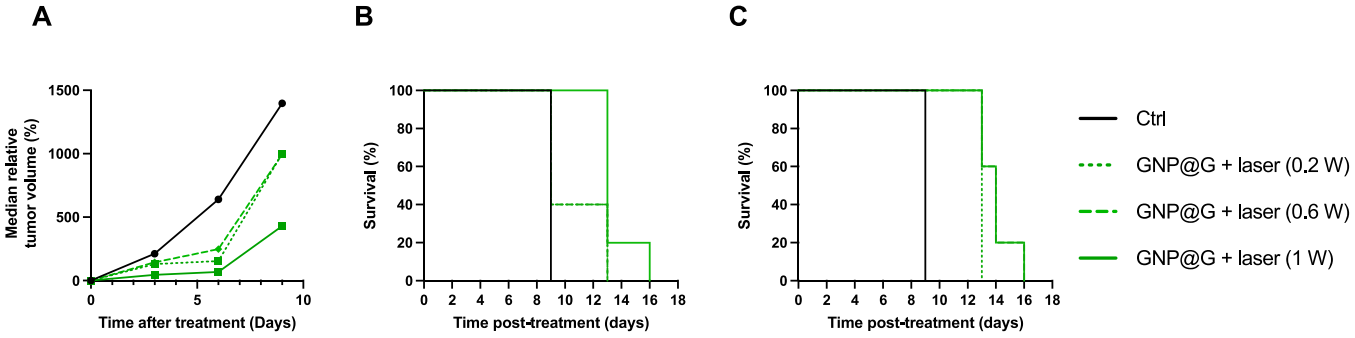

Figure 7. Effects of gGNP@G and laser irradiation on the tumor volume of mice bearing subcutaneous B16 murine melanoma xenograft and their survival. (A) Evolution of median relative tumor volume after treatment with 0.15 mg/mL GNP@G irradiated with NIR laser at different power. (B,C) Kaplan–Meier survival curve of mice treated with 0.15 mg/mL (B), or 0.3 mg/mL (C) irradiated with an NIR laser at different powers. Five mice per condition were included.

CBOP11 for 4 h before incubating them at different time points in a gGNP-free medium (Figure 5C). We observed a quick transferrin exocytosis (50% decrease of Tf-AF647 intensity after 5 min) and a slower exocytosis of gGNP@G and gGNP@G@CBOP11 (50% decrease in 30 min). This difference between transferrin and gGNP exocytosis could be explained by the intracellular trafficking of these two cargos. Transferrin is a very well-known cargo endocytosed by a clathrin-dependent pathway that is quickly recycled back at the plasma membrane.[60] Once internalized, gGNP@G and gGNP@G@CBOP11 are sorted in lysosomes before being exocytosed by electron-dense vesicles (Figure 3, right) suggesting a lysosomal exocytosis. Lysosomal exocytosis leads to lysosome excretion in order to clear the cell[61] and has already been involved in nanoparticle excretion.[62,63]

gGNP@G Is More Efficient In Vivo Than gGNP@G@CBOP11. Except for the 30 first minutes of internalization, there is no statistical difference between gGNP@G and gGNP@G@CBOP11 in terms of endocytosis ratio, cell type specificity, intracellular trafficking, and exocytosis. Therefore, both compounds have been accepted in preclinical tests.

For this comparison study, a unique power laser was used and was set up to 0.2 W/cm^2. Treated melanoma bearing mice did not show significant weight loss (the toxicity limit set by the National Cancer Institute (NCI) is −20%). The monitoring of tumor volume showed a significant antitumor activity of gGNP@G and gGNP@G@CBOP11 with a T/C ratio lower than 42 and 48% respectively at D6 (Figure 6).

The relative area under the curve was 55 and 67% which indicates a global inhibition of tumor proliferation of 45 and 33%. No regression was observed (Table 1). With the reference treatment: anti-PD1 mAb, no antitumor activity was observed (T/C > 42% and a relative area under the curve of 113% (Table 1) for 10 days of treatment.

gGNP@G Efficiency. To assess the efficiency of gGNP@G, several power lasers were tested: 0.2, 0.6, and 1 W and nanoparticles were used at 0.15 mg/mL. The relative areas under the curve are respectively 51, 57, and 21% for GNP@G combined with a laser treatment at 0.2, 0.6, and 1 W respectively (Figure 7A) that indicate a global inhibition of tumor proliferation of 49, 43, and 79%. No regression was observed (Table 2). Thus, a significant antitumor activity of gGNP@G combined to laser was observed with a T/C ratio lower than 42%.

The survival rate of mice treated with 0.15 mg/mL + 1 W, 0.3 mg/mL + 0.6 W, and 0.3 mg/mL + 1 W was significantly higher than that of control mice ($P < 0.05$) (Figure 7B,C).

Three days after the treatment, a crust on the tumor site of the mice treated with gGNP@G 0.3 mg/mL combined to a power laser of 1 W and in a mouse treated with gGNP@G 0.15 mg/mL combined to a power laser of 1 W was observed. An ulceration then appeared 3 to 6 days later with bleeding. No damage was observed on health skin irradiated with the laser.

Safety Studies. No in vitro and in vivo toxicity of gGNP@G was reported, as shown in Table 3

DISCUSSION

Previous studies from our team demonstrate the power of *Hubertia ambavilla* to reduce gold to obtain different shapes of gGNP (spherical or flower-shape) with different properties. In oncology, our effort strongly focused on the 15 nm spherical shape gGNP. Our team showed the interest of photothermal therapy using intratumorally injected gGNP@G@CBOP11 in subcutaneous melanomas in mice.[34,35] This study aimed to

https://doi.org/10.1021/acsomega.2c07054
ACS Omega 2023, 8, 4092−4105

Table 2. Antitumor Activity of gGNP@G against the Subcutaneous B16 Murine Melanoma Xenografts[a]

			inhibition of tumor growth		
compound	dose (mg/mL)	laser	optimal T/C[b] (%)	optimal T/C[b] (%)	activity rating[c]
gGNP@G	0.15	0.2	51	24	L
		0.6	57	39	L
		1	21	11	L
	0.30	0.2	89	74	0
		0.6	44	27	L
		1	19	13	L

[a]rAUC = relative area under the tumor growth curve (expressed as a percentage of the median area under the tumor growth curve of the control group). [b]T/C = (median tumor volume of drug-treated group/median tumor volume of control group) × 100; According to NCI criteria, a T/C ≤ 42% is the minimum level for activity.[33] The optimal T/C is the lowest value, reflecting the maximal tumor growth inhibition. [c]Activity Rating: "0": inactivity if T/C > 42%; "L": low level of activity if T/C ≤ 42%; "H": High level of activity if T/C ≤ 10%; "T": toxicity if body weight loss >20% or % presumed drug-related death >20%.[33]

compare three gGNP candidates, gGNP, gGNP@G, and gGNP@G@CBOP11, for their internalization, intracellular trafficking, exocytosis, specificity to cancerous cells, toxicity, and PTT efficiency before the translation to clinics. gGNPs, because of their slow, nonspecific internalization, were quickly abandoned. Addition of CBOP11 to gGNP@G is not worth it. It permitted to speed up gGNP internalization up to 30 min, but it does not change the final internalization ratio, the specificity to cancerous cells, the intracellular trafficking, or the exocytosis. On the contrary, it brings cytotoxicity and a decrease of gGNP stability (data not shown). Therefore, gGNP@G has been chosen to be tested in clinics.

Otto Warburg was the first one to show the glucose over-uptake of cancerous cells.[45] Since then, studies have shown an overexpression of GLUT1 and/or GLUT3 in different cancers,[64−66] which we confirmed here in skin cancer. Melanoma, basal cell carcinoma, and squamous cell carcinoma are the three main forms of skin cancer, representing more than 99% of the cases. Interestingly, it was previously shown that GLUT1 and GLUT3 expression was positively correlated with glucose uptake in malignant melanomas.[67] Therefore, GLUTs, especially GLUT1 and GLUT3, are more and more raising attention and start to be considered as a putative therapeutic target.[68] gGNP@G is a 15 nm gold core nanoparticle functionalized with glucose to target GLUT and optimize the endocytosis. Previous studies showed that functionalization of nanoparticles with glucose is an efficient way of targeting it.[69] In our case, gGNP@G internalization is dependent on glucose and permitted to have three times more nanoparticles in cancerous cells than in healthy cells. This intracellular concentration difference will permit to adjust the laser power to have an optimal heating to kill cancerous cells with no toxic effect in surrounding healthy cells.

Then, it was important to unravel the internalization pathways, the intracellular trafficking, and the externalization pathways involved in the gGNP@G journey in cells. Most of the studies focused only on the uptake of nanoparticles, and little is known about the intracellular trafficking and the nanoparticle excretion which could lead to unwanted toxicity.[70] For example, it is known that nanoparticles addressed to the nucleus could lead to acute toxicity because of interaction with DNA.[71] gGNP@G are internalized through a clathrin-dynamin-dependent endocytosis and addressed to lysosomes where they are finally excreted through lysosomal exocytosis. Interestingly, another team have shown very recently that GLUT-dependent endocytosed nanoparticles were also excreted through lysosomal exocytosis.[63]

Endocytosis and exocytosis are co-occurrent phenomena which are dependent on intracellular and extracellular concentration. In clinics, NIR irradiation needs to be applied when the intracellular concentration of gGNP is at its highest to optimize the heating. According to our results, timing between nanoparticle injection and NIR irradiation should be around 30−60 min with gGNP@G, which was validated by our physician partners.

The objective of the first in vivo study was to compare the effect of gGNP@G and gGNP@G@CBOP11. The study was done on a model of murine melanoma which is particularly aggressive (B16/F10), and nanoparticles were compared to reference treatment (anti-PD1 mAb). A significant antitumor activity was observed with the two nanoparticles while no activity was observed with the mAb. The antitumor effect was

Table 3. Results of Toxicology Studies Performed with gGNP@G

study title GLP status/ISO number	findings /endpoints
in vitro toxicology studies	
bacterial reverse mutation (Ames) assay GLP	no biologically significant increase in the revertant frequency in any strains in the absence or presence of S9 metabolic active
in vitro cytotoxicity test on L929 mammalian cells GLP/ISO 10993:5	undiluted and diluted gGNP@G formulations showed no toxicity (cytotoxicity grade 0 in all cases)
in vivo toxicology studies	
skin sensitization test (Local lymph node assay) GLP	- no mortality or signs of systemic toxicity were observed
	- there was no indication of irritation at the site of treatment
	- no gGNP@G-related effects were observed on the mean body weight of treated animal
	- treatment was shown to bear no sensitization potential
acute systemic toxicity study in mice GLP/ISO 10993:11	no systemic toxicity was observed after a single IV administration of the gGNP@G
a 16-day intramuscular toxicity study in rats followed by a 4-week recovery period GLP ISO 10993:11/ISO 10993:6	one gAuNP@G-treated male was found dead on day 13. The finding was considered to be incidental and not related to treatment with the test item. No systemic toxicity was observed after 2 IM administrations of the gold nanoparticles. No effects on body weight, food consumption, clinical pathology parameters, and organ weights. Repeated administrations of gAuNP@G were well tolerated
pyrogen detection assay GLP/ISO 1099:11	the product does not show the presence of pyrogens

https://doi.org/10.1021/acsomega.2c07054
ACS Omega 2023, 8, 4092−4105

higher with gGNP@G than with gGNP@G@CBOP11. Thus, it was decided to continue the efficiency studies only with gGNP@G modifying the irradiation parameters to get a higher hyperthermia thus leading to a higher antitumor activity.

Thus, in the following studies several combinations of dose and power laser were tested. The best results were obtained with 0.15 mg/mL associated with 1 W and with 0.3 mg/mL associated with 0.6 or 1 W. In addition, several preclinical safety studies showed that gGNP@G is well tolerated, not toxic, and biocompatible when injected in vivo. In conclusion, no toxic effects were observed either in vitro or in vivo.

We do believe that PTT using gGNP@G will become a powerful tool in the array at the disposal of physicians along with immunotherapy and targeted therapy in the treatment of melanoma and skin cancer in general. Combination of both PTT and immunotherapy could be considered especially regarding the results of few teams who show in mice the power of this combination, not only on the primary tumor but also on distant metastatic tumors.[72−76] This abscopal effect, usually observed with the combination of radiotherapy and immunotherapy, is still not completely understood but could be a solution to the bad prognosis of advanced metastatic melanoma. Besides the therapeutic effect, GNPs could also be a wonderful diagnostic tool as it is described in the literature.[77−79] Even if this study only focused on the therapeutic effect of photothermal therapy using our 15 nm round-shape gGNPs, this nanotheranostic shows strong potential for therapy in different kinds of cancer, using different properties of gGNPs (PTT, photodynamic therapy, drug carrier) as well as in diagnostics.

METHODS

GNP Synthesis and Coating. Tetrachloroauric(III) acid, trisodium citrate dihydrate, and D-(+)-Glucose were ordered from Sigma-Aldrich. The plant (TSK1) was purchased from CAHEB, Reunion Island. CBOP11 peptide was purchased from SynVec. Ultrapure water (18.2 MΩ cm, Millipore) was used for all procedures.

gGNP, gGNP@G, and gGNP@CBOP11 were prepared according to a previously described method.[34] In a nutshell: extract of dry *Hubertia ambavilla* leaves were dissolved in an aqueous acidic solution (pH 4). This solution was refluxed with vigorous stirring, in a flask equipped with a reflux condenser and protected from light. Then, once the fine droplets appeared on the walls, 4 mL of an aqueous solution of HAuCl4 was added very quickly. The solution turned red-brownish rapidly within a minute. The flask was then removed from the oil bath, and the solution remained under vigorous stirring for additional 15 min. The solution was finally kept at 4 °C, protected from light.

tGNPs were synthesized by following the "inversed Turkevich" method (i.e., chloroauric acid to citrate) proposed by Sivaraman et al. Briefly, to boiling solution (24.75 mL) of disodium citrate, 0.25 mL (25.4 mM) chloroauric acid was added. According to Kumar' model prediction, the molar ratio of sodium citrate solution to HAuCl4 was set to 2.5.[80] The solution mixture was stirred continuously for 15 min. After that, the solution was allowed to cool down to room temperature under stirring and then, was centrifuged. The precipitate was washed with ultrapure water.[81]

Microarray Gene Expression Data Extraction. Two data sets with more than 20 samples in a single microarray platform tested for gene expression in melanomas (GSE46517[49] and GSE114445[50]) were identified from the literature. Data were extracted and analyzed as previously described.[82] In a nutshell, there are URLs for individual data sets (data series as referred to on GEO) on the GEO website and for each data series, a link permits the access to the Series Matrix Files which contain the expression values for each gene (probeset) and each sample. Microarray gene expression data were retrieved from the data matrices deposited to GEO by the original authors. Data normalization methods were mentioned under each data series on GEO. Once the gene expression matrices were successfully obtained, expression values were extracted for GLUT1−4 and VEGFR1/2 encoding genes.

Cell Lines and siRNA Transfections. SK-MEL-28 cells were purchased from ATCC and were grown in Dulbecco's modified Eagle's medium (DMEM) (4.5 g/L) (Gibco) supplemented with 1% sodium pyruvate (Gibco), 1% Glutamax (Gibco), and 10% heat-inactivated FBS (Eurobio − CVFSVF00-0 U) at 5% CO_2 at 37 °C. Primary epidermal melanocytes, normal, human, adult (HEMa) (PCS-200-013), were purchased from ATCC and were grown according to the manufacturer's recommendations: in dermal cell basal medium (PCS-200-030) supplemented with adult melanocyte growth kit (PCS-200-042) at 5% CO_2 at 37 °C.

For siRNA transfection experiments, cells were transfected with the relevant siRNA at 10 nM final concentration (DNM2: GCAGCUCAUCUUCUCAAAATT; CHC: UAAUCCAAUUCGAAGACCAAU) by using Lipofectamine RNAiMAX (Invitrogen) the day before the experiment. The control condition was cells incubated with the same concentration of lipofectamine (2 μL/mL).

Immunoblotting. Total cell lysates were harvested by removing growth medium and adding Laemmli sample buffer (Bio-Rad) supplemented with β-mercaptoethanol. Samples were boiled for 5 min. Denatured proteins were loaded on 10% acrylamide Mini PROTEAN TGX precast gel (Bio-Rad). Separated proteins were transferred onto PVDF membrane by liquid transfer. Membranes were blocked with 3% (wtg/vol 100 mL) albumin from bovine serum (BSA, Sigma) at room temperature, before incubation with primary antibodies overnight at 4 °C, in 1% BSA. Incubation with the secondary horseradish peroxidase-conjugated IgG antibody was performed at room temperature. Blots were developed using Amersham ECL western blotting detection reagents and the Amersham Imager 600 (GE). The presented results are representative of at least three independent experiments.

Antibodies and Reagents. The following primary antibodies were used for immunofluorescence: mouse anti-LAMP1 (1/10.000) (H4A3 clone, Developmental Studies Hybridoma Bank), mouse anti-EEA1 (1/100) (Transduction Laboratories, 610456), mouse anti-RAB11 (1/100) (BD Transduction, 610,657). Donkey antimouse-AF647 (1/300) (Invitrogen A32787) antibody was used as a secondary antibody. DAPI (Sigma, D9542) at 0.1 μg/mL and HCS Cell Mask Blue Stain (1/400) (Invitrogen, H32720) were used to mark nuclei and cytoplasm. The following tagged transferrin was used: Tf-AF647 (1/1000) (Molecular Probes, T23366) and Tf-488 (1/1000) (Molecular Probes).

The following primary antibodies were used for immunoblotting: mouse anti-CHC (abcam ab2731) (1/500), goat anti-DNM2 (Santa Cruz, SC-6400) (1/1000), and rabbit anti-GAPDH (Sigma G9545) (1/6000). Goat antimouse-HRP (Amersham, NA931) (1/10000), rabbit anti-goat-HRP (Biodesign, W99119P) (1/10,000), and donkey antirabbit-HRP

https://doi.org/10.1021/acsomega.2c07054
ACS Omega 2023, 8, 4092−4105

(Amersham, NA9340) (1/10000) were used as secondary antibodies.

To measure cytotoxicity, the Cytotox96 Non-Radioactive cytotoxicity assay kit (Promega) measuring the extracellular LDH has been used after a 6 h incubation at a concentration of 6 nM.

Cultured Cell Incubation with GNPs. For experiments with SK-MEL-28 only, cells were seeded 24 h before the experiment on 24WP with (IF experiments) or without (FACS experiments) 12-mm coverslips at a density of 1×10^5 cells/well. For coculture experiments (Figure 5), cells were seeded 48-72 h before the experiment on 24WP at a density of 0.5×10^5 cells/well. Except for the study of the glucose impact, the following media were prepared: internalization medium (IM: DMEM 4.5 g/L supplemented with 0.2% BSA), GNP medium (dilution of GNP stock to have a final concentration of 3 or 6 nM in IM supplemented with 1/10 (v/v) of GNP with PBS 10× (Gibco) to compensate the lack of salt in GNP stock solution and supplemented or not with 1/2000 of Tf-AF647), and exocytosis medium (EM: IM supplemented with 5% heat-inactivated FBS). For the study of glucose impact on the internalization (Figure 2D), two different internalization media were prepared: IM-g− (DMEM 0 g/L supplemented with 0.2% BSA) and IM-g+ (IM-g− supplemented with 10 g/L of glucose (Sigma)). To study GNP endocytosis or intracellular trafficking, cells were washed twice with IM and then incubated for at least 30 min with IM. Then IM was replaced with diluted GNP solution at the desired concentration and temperature during the indicated time. For exocytosis experiments (Figure 3C), steps of washing and incubation during the indicated time with EM were added to this protocol.

Immunofluorescence, Image Acquisition, Analysis, and Quantification. SK-MEL-28 cells were incubated with GNP and Tf-AF647. At the end of the internalization or exocytosis experiments, cells were washed with PBS, fixed in PFA 4% in PBS for 30 min, then washed, and incubated with PBS BSA (0.1%) saponin (0.05%) for 30 min. Finally, cells were incubated with DAPI (Sigma, D9542) HCS (1/400) in PBS BSA saponin.

For colocalization experiments (Figure 5A,B), SK-MEL-28 cells were incubated with GNP or Tf-AF488 (1/1000) supplemented or not with Tf-AF647 (1/1000) for 4 h. Then, cells were washed and fixed with PFA 4% in PBS for 30 min, washed and incubated for 30 min in PBS BSA (0.1%) saponin (0.05%), washed and incubated for 1 h with a primary antibody anti-LAMP1, RAB11, or EEA1 in PBS BSA saponin, washed and incubated for 1 h with an antimouse-AF647, washed, and finally incubated for 1 h with DAPI (Sigma, D9542) and HCS (1/400) in PBS BSA saponin.

For image acquisition: a LSM700 inverted laser-scanning confocal microscope (Zeiss), with a 100×/1.4 oil immersion objective (Zeiss); an Axio Observer.Z1 microscope (Zeiss) equipped with a swept field confocal Opterra system (Bruker); and an Evolve 512 Delta EMCCD camera (Photometrics), using a 100× PlanAPO-CHROMAT oil immersion/1.4 N.A. objective (Zeiss). The following excitation/emission couples were acquired: 405−460/50 for DAPI/HCS, 488−535/50 for Tf-AF488, 561−535/50 for GNP, and 640−700/75 for AF647. Microscopy images were processed and quantified with ICY software[83] (http://icy.bioimageanalysis.org). Colocalization quantification was performed on confocal images using the distance analysis plugin in ICY software. GNP and Tf-AF647 endocytosis were quantified with ICY software using "HK-Means" and "Active Contours" plugins to automatically detect cell boundaries and "Spot Detector" plugin to measure the number of GNP and Tf-AF647 spots within the detected cells. The total intensity of GNP and Tf-AF647 spots was normalized to the mean value of the time 0 (Figures 2C and 5C), to the 0 g/L of glucose condition (Figure 2D) or to the not transfected samples (Figure 2F,H).

Transmission Electron Microscopy. Cells incubated with GNP were fixed in 2.5% glutaraldehyde (Sigma-Aldrich) in PHEM buffer 1× for 1 h at room temperature. Fixed samples were washed three times by the addition of fresh 0.1 M PHEM buffer and postfixed in 1% osmium (EMS) in 0.1 M PHEM buffer for 1 h. Samples were gradually dehydrated in ethanol (Sigma-Aldrich) series from 50 to 100%. Samples were embedded in epoxy resin (EMS), followed by polymerization for 48 h at 60 °C. Ultrathin sections (70 nm) were cut with a Leica UC7 microtome and stained with 4% uranyl acetate for 45 min followed by lead citrate for 10 min. Sections were observed using a TEM Thermo Fisher Tecnai T12 at 120 kV.

Flow Cytometry and Data Analysis. Incubated cells were detached using PBS supplemented with EDTA (Invitrogen) or trypsin (Sigma − 59427C) diluted in PBS to a final concentration of 1% for 5 min at 37 °C, and then neutralized with PBS supplemented with 5% FBS. Cells were centrifuged (5 min, 1200 RPM, 4 °C), supernatants were removed, and the pellet was resuspended in PFA 4% diluted in PBS for 1 h at 4 °C. Cells were washed and finally run in an Attune NxT Flow Cytometer (Thermo Fisher Scientific) recording FSC, SSC, and YL2 channels. The geometrical mean fluorescence of intracellular GNP was measured in gated cells in the YL2 channel using flowjo software. Data were normalized to the GNP@G@CBOP11 at 30 min in SK-MEL-28 condition.

In Vivo Experiments. *Nanoparticles.* gGNP@G and gGNP@G@CBOP11 were used at a concentration of 0.15 or 0.3 mg/mL. For experiment, nanoparticles were injected directly into the tumors with a volume corresponding to 20% of the tumor volume.

Treatment of Reference. Anti-PD1 mAb at 5 mg/kg (ip injection every 5 days) was used as reference treatment.

Tumor Cell Lines. B16 is a murine melanoma cell line from a C57Bl/6 J mouse. The cell line was cultured in RPMI 1640 medium supplemented with heat-inactivated FBS (10%). Cells are maintained in an incubator at 37 °C with 5% CO_2.

Mice. Female C57Bl/6 mice, 6 week-old were used. 1×10^5 B16 cells in 100 μL NaCl 0.9% were subcutaneously injected in the right flank of the mice. For antitumor effect assessment, mice were weighed, and tumors were measured every 3 days until the mice died or the tumor volume reached 1500 mm^3 or the weight loss was upper than 20% of the initial weight.

Evaluation of Toxic-Side Effects. Maximum weight losses or gains, expressed as a percentage of the initial body weight of the experimental animals, were used to provide an assessment of the toxicity of both gGNPs. According to NCI criteria, a dose is considered toxic if the induced body weight loss is higher than 20% of the initial mouse body weight. It should be remembered that these weights also include the weight of the tumors, which increases with time.

Photothermal Therapy. Mice were anesthetized with 2.5% isoflurane and a subcutaneous injection of buprenorphine (0.1 mg/kg) was done. After that, tumors were measured, and nanoparticles were injected in the center of the tumor with an

https://doi.org/10.1021/acsomega.2c07054
ACS Omega 2023, 8, 4092−4105

insulin syringe 31G. One hour later, mice were placed under the medical laser (Hyper diode 808, Hyper Photonics, Italy) for treatment with the following settings: Wavelength: 808 nm, power: variable from 0.2 to 1 W, duration: 10 min, and irradiated surface: 3.93cm^2 (diameter of the probe: 2.5 cm).

Evaluation of Antitumor Activity/Tumor Growth. Treatment efficacy was assessed in terms of the compound's effects on tumor volume for PTT-treated mice relative to control vehicle-treated mice. Two evaluation criteria were used in parallel: (i) Growth inhibition, calculated as the ratio of the median tumor volume of treated versus control groups: T/C, % = (median tumor volume of treated group on day X/median tumor volume of control group on day X) × 100, the optimal value, being the minimal T/C ratio which reflects the maximal tumor growth inhibition achieved;[84] (ii) relative area under the tumor growth curve, rAUC (%), representative of the tumor growth curve as a whole, reflects the overall effect of a test compound over time.[85] rAUC = [(area under the tumor volume growth curve of the treated group/median area under the tumor volume growth curve of the control group) × 100]. The more active the compound, the lower the rAUC value.

The tumor volume was monitored by measuring the tumors with a digital caliper and according to the formula $(L \times l^2)/2$.

Statistical Analysis. Data were presented as median. Comparison among groups in the survival data was made using the log-rank test.

Ethic Approval. All procedures have been evaluated and approved by an ethic committee (Agreement number A974 001; Comité d'éthique du CYROI number 114; Cyclotron Reunion Océan Indien, Sainte Clotilde, Reunion Island) and authorized by the French Ministry of Education and Research (Reference number APAFIS#28417-2020100114549534_v3).

Data Presentation and Statistical Analysis. Prism 8.4.3 (GraphPad Software) was used to perform statistical analysis. Results are represented as mean ± SD, except as otherwise indicated. Welch's *t* test performed as unpaired two-tailed analysis was used as statistical analysis. $P < 0.05$ was considered significant for all analyses.

■ ASSOCIATED CONTENT

Supporting Information

The Supporting Information is available free of charge at https://pubs.acs.org/doi/10.1021/acsomega.2c07054.

Supplementary methods, Figure S1: Physico-chemical characterization of gold nanoparticles, Figure S2: GLUT1−4 and VEGFR1/2 encoding gene expression in cutaneous squamous cell carcinoma, and Figure S3: GLUT1−4 and VEGFR1/2 encoding gene expression in cutaneous basal cell carcinoma (PDF)

■ AUTHOR INFORMATION

Corresponding Authors

Anne-Laure Morel − *Torskal, 97490 Sainte-Clotilde, France*; Email: annelaure.morel@torskal.com

Nathalie Sauvonnet − *Group Intracellular Trafficking and Tissue Homeostasis, Institut Pasteur, Université Paris Cité, 75015 Paris, France*; orcid.org/0000-0003-0306-3376; Email: nathalie.sauvonnet@pasteur.fr

Authors

Clément Bonamy − *Torskal, 97490 Sainte-Clotilde, France; Group Intracellular Trafficking and Tissue Homeostasis, Institut Pasteur, Université Paris Cité, 75015 Paris, France*

Sabrina Pesnel − *Torskal, 97490 Sainte-Clotilde, France*; orcid.org/0000-0001-7839-4394

Maroua Ben Haddada − *Torskal, 97490 Sainte-Clotilde, France*

Olivier Gorgette − *Ultrastructural BioImaging, Institut Pasteur, Université Paris Cité, 75015 Paris, France*

Christine Schmitt − *Ultrastructural BioImaging, Institut Pasteur, Université Paris Cité, 75015 Paris, France*

Complete contact information is available at: https://pubs.acs.org/10.1021/acsomega.2c07054

Author Contributions

‖C.B. and S.P. contributed equally to this study.

Notes

The authors declare no competing financial interest.

■ ACKNOWLEDGMENTS

We thank Valérie Malardé for technical help on the project. We thank ASSU 2000 for supporting NS. We are grateful for support for UBI equipment from the French Government Programme Investissements d'Avenir France BioImaging (FBI, N° ANR-10-INSB-04-01) and the French gouvernement (Agence Nationale de la Recherche) Investissement d'Avenir programme, Laboratoire d'Excellence "Integrative Biology of Emerging Infectious Diseases" (ANR-10-LABX-62-IBEID).

■ REFERENCES

(1) Apalla, Z.; Nashan, D.; Weller, R.; Castellsagué, X. Skin Cancer: Epidemiology, Disease Burden, Pathophysiology, Diagnosis, and Therapeutic Approaches. *Dermatol. Ther.* **2017**, *7*, s5−s19.

(2) Qureshi, A. A.; Wei-Passanese, E. X.; Li, T.; Han, J. Host Risk Factors for the Development of Multiple Non-Melanoma Skin Cancers. *J. Eur. Acad. Dermatol. Venereol.* **2013**, *27*, 565−570.

(3) Leiter, U.; Garbe, C. Epidemiology of Melanoma and Nonmelanoma Skin Cancer—the Role of Sunlight. *Adv. Exp. Med. Biol.* **2008**, *624*, 89−103.

(4) Conic, R. Z.; Cabrera, C. I.; Khorana, A. A.; Gastman, B. R. Determination of the Impact of Melanoma Surgical Timing on Survival Using the National Cancer Database. *J. Am. Acad. Dermatol.* **2018**, *78*, 40.e7−46.e7.

(5) Rebecca, V. W.; Sondak, V. K.; Smalley, K. S. M. A Brief History of Melanoma: From Mummies to Mutations. *Melanoma Res.* **2012**, *22*, 114−122.

(6) Robert, C.; Grob, J. J.; Stroyakovskiy, D.; Karaszewska, B.; Hauschild, A.; Levchenko, E.; Chiarion Sileni, V.; Schachter, J.; Garbe, C.; Bondarenko, I.; Gogas, H.; Mandalá, M.; Haanen, J. B. A. G.; Lebbé, C.; Mackiewicz, A.; Rutkowski, P.; Nathan, P. D.; Ribas, A.; Davies, M. A.; Flaherty, K. T.; Burgess, P.; Tan, M.; Gasal, E.; Voi, M.; Schadendorf, D.; Long, G. V. Five-Year Outcomes with Dabrafenib plus Trametinib in Metastatic Melanoma. *N. Engl. J. Med.* **2019**, *381*, 626−636.

(7) Nomura, S.; Morimoto, Y.; Tsujimoto, H.; Arake, M.; Harada, M.; Saitoh, D.; Hara, I.; Ozeki, E.; Satoh, A.; Takayama, E.; Hase, K.; Kishi, Y.; Ueno, H. Highly Reliable, Targeted Photothermal Cancer Therapy Combined with Thermal Dosimetry Using a near-Infrared Absorbent. *Sci. Rep.* **2020**, *10*, 9765.

(8) Huang, X.; El-Sayed, M. A. Gold Nanoparticles: Optical Properties and Implementations in Cancer Diagnosis and Photothermal Therapy. *J. Adv. Res.* **2010**, *1*, 13−28.

(9) Stern, J. M.; Kibanov Solomonov, V. V.; Sazykina, E.; Schwartz, J. A.; Gad, S. C.; Goodrich, G. P. Initial Evaluation of the Safety of

Nanoshell-Directed Photothermal Therapy in the Treatment of Prostate Disease. *Int. J. Toxicol.* **2016**, *35*, 38−46.
(10) Rastinehad, A. R.; Anastos, H.; Wajswol, E.; Winoker, J. S.; Sfakianos, J. P.; Doppalapudi, S. K.; Carrick, M. R.; Knauer, C. J.; Taouli, B.; Lewis, S. C.; Tewari, A. K.; Schwartz, J. A.; Canfield, S. E.; George, A. K.; West, J. L.; Halas, N. J. Gold Nanoshell-Localized Photothermal Ablation of Prostate Tumors in a Clinical Pilot Device Study. *Proc. Natl. Acad. Sci. U. S. A.* **2019**, *116*, 18590−18596.
(11) Paithankar, D. Y.; Sakamoto, F. H.; Farinelli, W. A.; Kositratna, G.; Blomgren, R. D.; Meyer, T. J.; Faupel, L. J.; Kauvar, A. N. B.; Lloyd, J. R.; Cheung, W. L.; Owczarek, W. D.; Suwalska, A. M.; Kochanska, K. B.; Nawrocka, A. K.; Paluchowska, E. B.; Podolec, K. M.; Pirowska, M. M.; Wojas-Pelc, A. B.; Anderson, R. R. Acne Treatment Based on Selective Photothermolysis of Sebaceous Follicles with Topically Delivered Light-Absorbing Gold Microparticles. *J. Invest. Dermatol.* **2015**, *135*, 1727−1734.
(12) Uboldi, C.; Bonacchi, D.; Lorenzi, G.; Iris, M. I.; Pohl, C.; Baldi, G.; Unger, R. E.; James, C. J. Gold Nanoparticles Induce Cytotoxicity in the Alveolar Type-II Cell Lines A549 and NCIH441. *Part. Fibre Toxicol.* **2009**, *6*, 18.
(13) Connor, E. E.; Mwamuka, J.; Gole, A.; Murphy, C. J.; Wyatt, M. D. Gold Nanoparticles Are Taken up by Human Cells but Do Not Cause Acute Cytotoxicity. *Small* **2005**, *1*, 325−327.
(14) Vijayakumar, S.; Ganesan, S. In Vitro Cytotoxicity Assay on Gold Nanoparticles with Different Stabilizing Agents. *J. Nanomater.* **2012**, *2012*, No. 734398.
(15) Pan, Y.; Neuss, S.; Leifert, A.; Fischler, M.; Wen, F.; Simon, U.; Schmid, G.; Brandau, W.; Jahnen-Dechent, W. Size-Dependent Cytotoxicity of Gold Nanoparticles. *Small* **2007**, *3*, 1941−1949.
(16) Chou, L. Y. T.; Chan, W. C. W. Fluorescence-Tagged Gold Nanoparticles for Rapidly Characterizing the Size-Dependent Biodistribution in Tumor Models. *Adv. Healthcare Mater.* **2012**, *1*, 714−721.
(17) Huo, S.; Ma, H.; Huang, K.; Liu, J.; Wei, T.; Jin, S.; Zhang, J.; He, S.; Liang, X. J. Superior Penetration and Retention Behavior of 50 Nm Gold Nanoparticles in Tumors. *Cancer Res.* **2013**, *73*, 319−330.
(18) Gao, H.; Shi, W.; Freund, L. B. Mechanics of Receptor-Mediated Endocytosis. *Proc. Natl. Acad. Sci. U. S. A.* **2005**, *102*, 9469−9474.
(19) Jiang, W.; Kim, B. Y. S.; Rutka, J. T.; Chan, W. C. W. Nanoparticle-Mediated Cellular Response Is Size-Dependent. *Nat. Nanotechnol.* **2008**, *3*, 145−150.
(20) Zhang, G.; Yang, Z.; Lu, W.; Zhang, R.; Huang, Q.; Tian, M.; Li, L.; Liang, D.; Li, C. Influence of Anchoring Ligands and Particle Size on the Colloidal Stability and in Vivo Biodistribution of Polyethylene Glycol-Coated Gold Nanoparticles in Tumor-Xenografted Mice. *Biomaterials* **2009**, *30*, 1928−1936.
(21) Chithrani, B. D.; Chan, W. C. W. Elucidating the Mechanism of Cellular Uptake and Removal of Protein-Coated Gold Nanoparticles of Different Sizes and Shapes. *Nano Lett.* **2007**, *7*, 1542−1550.
(22) Enea, M.; Araújo, A. M.; de Almeida, M. P.; Soares, M. E.; Gonçalves-Monteiro, S.; de Pinho, P. G.; Pereira, E.; de L. Bastos, M.; Carmo, H. A Metabolomic Approach for the in Vivo Study of Gold Nanospheres and Nanostars after a Single-Dose Intravenous Administration to Wistar Rats. *Nanomaterials* **2019**, *9*, 1606.
(23) Tarantola, M.; Pietuch, A.; Schneider, D.; Rother, J.; Sunnick, E.; Rosman, C.; Pierrat, S.; Sönnichsen, C.; Wegener, J.; Janshoff, A. Toxicity of Gold-Nanoparticles: Synergistic Effects of Shape and Surface Functionalization on Micromotility of Epithelial Cells. *Nanotoxicology* **2011**, *5*, 254−268.
(24) Bartczak, D.; Muskens, O. L.; Nitti, S.; Sanchez-Elsner, T.; Millar, T. M.; Kanaras, A. G. Interactions of Human Endothelial Cells with Gold Nanoparticles of Different Morphologies. *Small* **2012**, *8*, 122−130.
(25) Schaeublin, N. M.; Braydich-Stolle, L. K.; Maurer, E. I.; Park, K.; MacCuspie, R. I.; Afrooz, A. R. M. N.; Vaia, R. A.; Saleh, N. B.; Hussain, S. M. Does Shape Matter? Bioeffects of Gold Nanomaterials in a Human Skin Cell Model. *Langmuir* **2012**, *28*, 3248−3258.
(26) Goodman, C. M.; McCusker, C. D.; Yilmaz, T.; Rotello, V. M. Toxicity of Gold Nanoparticles Functionalized with Cationic and Anionic Side Chains. *Bioconjugate Chem.* **2004**, *15*, 897−900.
(27) Pérez-Hernández, M.; Moros, M.; Stepien, G.; del Pino, P.; Menao, S.; De Las Heras, M.; Arias, M.; Mitchell, S. G.; Pelaz, B.; Gálvez, E. M.; De La Fuente, J. M.; Pardo, J. Multiparametric Analysis of Anti-Proliferative and Apoptotic Effects of Gold Nanoprisms on Mouse and Human Primary and Transformed Cells, Biodistribution and Toxicity in Vivo. *Part. Fibre Toxicol.* **2017**, *14*, 41.
(28) Tzror-Azankot, C.; Dreifuss, T.; Ben-Gal, T.-S.; Jacob, A.; Sadan, T.; Motiei, M.; Popovtzer, R. Cellular Internalization Pathways of Glucose-Functionalized Gold Nanoparticles. In *Proc. SPIE*, 2019.
(29) Hauck, T. S.; Ghazani, A. A.; Chan, W. C. W. Assessing the Effect of Surface Chemistry on Gold Nanorod Uptake, Toxicity, and Gene Expression in Mammalian Cells. *Small* **2008**, *4*, 153−159.
(30) Morel, A.-L.; Giraud, S.; Bialecki, A.; Moustaoui, H.; Lamy de La Chapelle, M.; Spadavecchia, J. Green Extraction of Endemic Plants to Synthesize Gold Nanoparticles for Theranostic Applications. *Front. Lab. Med.* **2017**, *1*, 158−171.
(31) Morel, A.-L. *Wo 2017/125695: Nanoparticules D'or Et Procede Ecologique De Preparation*, 2015.
(32) Zhang, S.; Li, J.; Lykotrafitis, G.; Bao, G.; Suresh, S. Size-Dependent Endocytosis of Nanoparticles. *Adv. Mater.* **2009**, *21*, 419−424.
(33) Corbett, T. H.; Valeriote, F. A.; Demchik, L.; Polin, L.; Panchapor, C.; Pugh, S.; White, K.; Knight, J.; Jones, J.; Jones, L.; LoRusso, P.; Foster, B.; Wiegand, R. A.; Lisow, L.; Golakoti, T.; Heltzel, C. E.; Ogino, J.; Patterson, G. M.; Moore, R. E. Preclinical anticancer activity of cryptophycin-8. *J. Exp. Ther. Oncol.* **1996**, *1*, 95−108.
(34) Ben Haddada, M.; Koshel, D.; Yang, Z.; Fu, W.; Spadavecchia, J.; Pesnel, S.; Morel, A. Proof of Concept of Plasmonic Thermal Destruction of Surface Cancers by Gold Nanoparticles Obtained by Green Chemistry. *Colloids Surf., B* **2019**, *184*, No. 110496.
(35) Pesnel, S.; Zhang, Y.; Weiling, F.; Morel, A. L. Dataset Concerning Plasmonic Thermal Destruction of Murine Melanoma by Gold Nanoparticles Obtained by Green Chemistry. *Data Brief* **2020**, *29*, No. 105370.
(36) Moros, M.; Pelaz, B.; López-Larrubia, P.; García-Martin, M. L.; Grazú, V.; De La Fuente, J. M. Engineering Biofunctional Magnetic Nanoparticles for Biotechnological Applications. *Nanoscale* **2010**, *2*, 1746−1755.
(37) Murray, R. A.; Qiu, Y.; Chiodo, F.; Marradi, M.; Penadés, S.; Moya, S. E. A Quantitative Study of the Intracellular Dynamics of Fluorescently Labelled Glyco-Gold Nanoparticles via Fluorescence Correlation Spectroscopy. *Small* **2014**, *10*, 2602−2610.
(38) Compostella, F.; Pitirollo, O.; Silvestri, A.; Polito, L. Glyco-Gold Nanoparticles: Synthesis and Applications. *Beilstein J. Org. Chem.* **2017**, *13*, 1008−1021.
(39) Turkevich, J.; Stevenson, P. C.; Hillier, J. A Study of the Nucleation and Growth Processes in the Synthesis of Colloidal Gold. *Discuss. Faraday Soc.* **1951**, *11*, 55−75.
(40) Garcia, M. A.; De La Venta, J.; Crespo, P.; Llopis, J.; Penadés, S.; Fernández, A.; Hernando, A. Surface Plasmon Resonance of Capped Au Nanoparticles. *Phys. Rev. B: Condens. Matter Mater. Phys.* **2005**, *72*, No. 241403.
(41) Choi, S. Y.; Jeong, S.; Jang, S. H.; Park, J.; Park, J. H.; Ock, K. S.; Lee, S. Y.; Joo, S. W. In Vitro Toxicity of Serum Protein-Adsorbed Citrate-Reduced Gold Nanoparticles in Human Lung Adenocarcinoma Cells. *Toxicol. In Vitro* **2012**, *26*, 229−237.
(42) Vetten, M. A.; Tlotleng, N.; Tanner Rascher, D.; Skepu, A.; Keter, F. K.; Boodhia, K.; Koekemoer, L. A.; Andraos, C.; Tshikhudo, R.; Gulumian, M. Label-Free in Vitro Toxicity and Uptake Assessment of Citrate Stabilised Gold Nanoparticles in Three Cell Lines. *Part. Fibre Toxicol.* **2013**, *10*, 50.
(43) Pernodet, N.; Fang, X.; Sun, Y.; Bakhtina, A.; Ramakrishnan, A.; Sokolov, J.; Ulman, A.; Rafailovich, M. Adverse Effects of Citrate/Gold Nanoparticles on Human Dermal Fibroblasts. *Small* **2006**, *2*, 766−773.

https://doi.org/10.1021/acsomega.2c07054
ACS Omega 2023, 8, 4092−4105

(44) Patra, H. K.; Banerjee, S.; Chaudhuri, U.; Lahiri, P.; Dasgupta, A. K. Cell Selective Response to Gold Nanoparticles. *Nanomedicine* **2007**, *3*, 111−119.
(45) Warburg, O.; Wind, F.; Negelein, E. The Metabolism of Tumors in the Body. *J. Gen. Physiol.* **1927**, *8*, 519−530.
(46) Hanahan, D.; Weinberg, R. A. Hallmarks of Cancer: The next Generation. *Cell* **2011**, *144*, 646−674.
(47) Hicklin, D. J.; Ellis, L. M. Role of the Vascular Endothelial Growth Factor Pathway in Tumor Growth and Angiogenesis. *J. Clin. Oncol.* **2005**, *23*, 1011−1027.
(48) Wu, Y.; Hooper, A. T.; Zhong, Z.; Witte, L.; Bohlen, P.; Rafii, S.; Hicklin, D. J. The Vascular Endothelial Growth Factor Receptor (VEGFR-1) Supports Growth and Survival of Human Breast Carcinoma. *Int. J. Cancer* **2006**, *119*, 1519−1529.
(49) Kabbarah, O.; Nogueira, C.; Feng, B.; Nazarian, R. M.; Bosenberg, M.; Wu, M.; Scott, K. L.; Kwong, L. N.; Xiao, Y.; Cordon-Cardo, C.; Granter, S. R.; Ramaswamy, S.; Golub, T.; Duncan, L. M.; Wagner, S. N.; Brennan, C.; Chin, L. Integrative Genome Comparison of Primary and Metastatic Melanomas. *PLoS One* **2010**, *5*, No. e10770.
(50) Yan, B. Y.; Garcet, S.; Gulati, N.; Kiecker, F.; Fuentes-Duculan, J.; Gilleaudeau, P.; Sullivan-Whalen, M.; Shemer, A.; Mitsui, H.; Krueger, J. G. Novel Immune Signatures Associated with Dysplastic Naevi and Primary Cutaneous Melanoma in Human Skin. *Exp. Dermatol.* **2019**, *28*, 35−44.
(51) Hameetman, L.; Commandeur, S.; Bavinck, J. N. B.; Wisgerhof, H. C.; de Gruijl, F. R.; Willemze, R.; Mullenders, L.; Tensen, C. P.; Vrieling, H. Molecular Profiling of Cutaneous Squamous Cell Carcinomas and Actinic Keratoses from Organ Transplant Recipients. *BMC Cancer* **2013**, *13*, 58.
(52) Jee, B. A.; Lim, H.; Kwon, S. M.; Jo, Y.; Park, M. C.; Lee, I. J.; Woo, H. G. Molecular Classification of Basal Cell Carcinoma of Skin by Gene Expression Profiling. *Mol. Carcinog.* **2015**, *54*, 1605−1612.
(53) Jee, B. A.; Lim, H.; Kwon, S. M.; Jo, Y.; Park, M. C.; Lee, I. J.; Woo, H. G. Molecular Classification of Basal Cell Carcinoma of Skin by Gene Expression Profiling. *Mol. Carcinog.* **2015**, *54*, 1605−1612.
(54) Kim, C. S.; Li, X.; Jiang, Y.; Yan, B.; Tonga, G. Y.; Ray, M.; Solfiell, D. J.; Rotello, V. M. Cellular Imaging of Endosome Entrapped Small Gold Nanoparticles. *MethodsX* **2015**, *2*, 306−315.
(55) Antonescu, C. N.; Foti, M.; Sauvonnet, N.; Klip, A. Ready, Set, Internalize: Mechanisms and Regulation of GLUT4 Endocytosis. *Biosci. Rep.* **2009**, *29*, 1−11.
(56) Eyster, C. A.; Higginson, J. D.; Huebner, R.; Porat-Shliom, N.; Weigert, R.; Wu, W. W.; Shen, R. F.; Donaldson, J. G. Discovery of New Cargo Proteins That Enter Cells through Clathrin-Independent Endocytosis. *Traffic* **2009**, *10*, 590−599.
(57) Wu, N.; Zheng, B.; Shaywitz, A.; Dagon, Y.; Tower, C.; Bellinger, G.; Shen, C. H.; Wen, J.; Asara, J.; McGraw, T. E.; Kahn, B. B.; Cantley, L. C. AMPK-Dependent Degradation of TXNIP upon Energy Stress Leads to Enhanced Glucose Uptake via GLUT1. *Mol. Cell* **2013**, *49*, 1167−1175.
(58) Thoidis, G.; Kupriyanova, T.; Cunningham, J. M.; Chen, P.; Cadel, S.; Foulon, T.; Cohen, P.; Fine, R. E.; Kandror, K. V. Glucose Transporter Glut3 Is Targeted to Secretory Vesicles in Neurons and PC12 Cells. *J. Biol. Chem.* **1999**, *274*, 14062−14066.
(59) Lampugnani, M. G.; Orsenigo, F.; Gagliani, M. C.; Tacchetti, C.; Dejana, E. Vascular Endothelial Cadherin Controls VEGFR-2 Internalization and Signaling from Intracellular Compartments. *J. Cell Biol.* **2006**, *174*, 593−604.
(60) Mayle, K. M.; Le, A. M.; Kamei, D. T. The Intracellular Trafficking Pathway of Transferrin. *Biochim. Biophys. Acta* **2012**, *1820*, 264−281.
(61) Buratta, S.; Tancini, B.; Sagini, K.; Delo, F.; Chiaradia, E.; Urbanelli, L.; Emiliani, C. Lysosomal Exocytosis, Exosome Release and Secretory Autophagy: The Autophagic- and Endo-Lysosomal Systems Go Extracellular. *Int. J. Mol. Sci.* **2020**, *21*, 2576.
(62) Yanes, R. E.; Tarn, D.; Hwang, A. A.; Ferris, D. P.; Sherman, S. P.; Thomas, C. R.; Lu, J.; Pyle, A. D.; Zink, J. I.; Tamanoi, F. Involvement of Lysosomal Exocytosis in the Excretion of Mesoporous Silica Nanoparticles and Enhancement of the Drug Delivery Effect by Exocytosis Inhibition. *Small* **2013**, *9*, 697−704.
(63) Wang, H.; Zhang, Z.; Guan, J.; Lu, W.; Zhan, C. Unraveling GLUT-mediated Transcytosis Pathway of Glycosylated Nanodisks. *Asian J. Pharm. Sci.* **2021**, *16*, 120−128.
(64) Flavahan, W. A.; Wu, Q.; Hitomi, M.; Rahim, N.; Kim, Y.; Sloan, A. E.; Weil, R. J.; Nakano, I.; Sarkaria, J. N.; Stringer, B. W.; Day, B. W.; Li, M.; Lathia, J. D.; Rich, J. N.; Hjelmeland, A. B. Brain Tumor Initiating Cells Adapt to Restricted Nutrition through Preferential Glucose Uptake. *Nat. Neurosci.* **2013**, *16*, 1373−1382.
(65) Brown, R. S.; Wahl, R. L. Overexpression of Glut-1 Glucose Transporter in Human Breast Cancer an Immunohistochemical Study. *Cancer* **1993**, *72*, 2979−2985.
(66) Han, A. L.; Veeneman, B. A.; El-Sawy, L.; Day, K. C.; Day, M. L.; Tomlins, S. A.; Keller, E. T. Fibulin-3 Promotes Muscle-Invasive Bladder Cancer. *Oncogene* **2017**, *36*, 5243−5251.
(67) Park, S. G.; Lee, J. H.; Lee, W. A.; Han, K. M. Biologic Correlation between Glucose Transporters, Hexokinase-II, Ki-67 and FDG Uptake in Malignant Melanoma. *Nucl. Med. Biol.* **2012**, *39*, 1167−1172.
(68) Ancey, P. B.; Contat, C.; Meylan, E. Glucose Transporters in Cancer − from Tumor Cells to the Tumor Microenvironment. *FEBS J.* **2018**, *285*, 2926−2943.
(69) Venturelli, L.; Nappini, S.; Bulfoni, M.; Gianfranceschi, G.; Dal Zilio, S.; Coceano, G.; Del Ben, F.; Turetta, M.; Scoles, G.; Vaccari, L.; Cesselli, D.; Cojoc, D. Glucose Is a Key Driver for GLUT1-Mediated Nanoparticles Internalization in Breast Cancer Cells. *Sci. Rep.* **2016**, *6*, 21629.
(70) Sakhtianchi, R.; Minchin, R. F.; Lee, K. B.; Alkilany, A. M.; Serpooshan, V.; Mahmoudi, M. Exocytosis of Nanoparticles from Cells: Role in Cellular Retention and Toxicity. *Adv. Colloid Interface Sci.* **2013**, *201*−*202*, 18−29.
(71) Tsoli, M.; Kuhn, H.; Brandau, W.; Esche, H.; Schmid, G. Cellular Uptake and Toxicity of Au55 Clusters. *Small* **2005**, *1*, 841−844.
(72) Yilmaz, M. T.; Elmali, A.; Yazici, G. Abscopal Effect, From Myth to Reality: From Radiation Oncologists' Perspective. *Cureus* **2019**, *11*, 9−13.
(73) Huang, L.; Li, Y.; Du, Y.; Zhang, Y.; Wang, X.; Ding, Y.; Yang, X.; Meng, F.; Tu, J.; Luo, L.; Sun, C. Mild Photothermal Therapy Potentiates Anti-PD-L1 Treatment for Immunologically Cold Tumors via an All-in-One and All-in-Control Strategy. *Nat. Commun.* **2019**, *10*, 4871.
(74) Chen, W.; Qin, M.; Chen, X.; Wang, Q.; Zhang, Z.; Sun, X. Combining Photothermal Therapy and Immunotherapy against Melanoma by Polydopamine-Coated Al2O3 Nanoparticles. *Theranostics* **2018**, *8*, 2229−2241.
(75) Zhang, N.; Song, J.; Liu, Y.; Liu, M.; Zhang, L.; Sheng, D.; Deng, L.; Yi, H.; Wu, M.; Zheng, Y.; Wang, Z.; Yang, Z. Photothermal Therapy Mediated by Phase-Transformation Nanoparticles Facilitates Delivery of Anti-PD1 Antibody and Synergizes with Antitumor Immunotherapy for Melanoma. *J. Controlled Release* **2019**, *306*, 15−28.
(76) Chen, Q.; Hu, Q.; Dukhovlinova, E.; Chen, G.; Ahn, S.; Wang, C.; Ogunnaike, E. A.; Ligler, F. S.; Dotti, G.; Gu, Z. Photothermal Therapy Promotes Tumor Infiltration and Antitumor Activity of CAR T Cells. *Adv. Mater.* **2019**, *31*, No. e1900192.
(77) Essa, B. M.; El-Hashash, M. A.; El-Mohty, A. A.; Sakr, T. M. *Egyptian Journal of Pure and Applied Science 99m Tc-Citrate-Gold Nanoparticles as a Tumor Tracer: Synthesis, Characterization, Radiolabeling and in-Vivo Studies*, 2019; Vol. *57*.
(78) Frantellizzi, V.; Verrina, V.; Raso, C.; Pontico, M.; Petronella, F.; Bertana, V.; Ballesio, A.; Marasso, S. L.; Miglietta, S.; Rosa, P.; Scibetta, S.; Petrozza, V.; de Feo, M. S.; de Vincentis, G.; Calogero, A.; Pani, R.; Perotto, G.; de Sio, L. 99mTc-Labeled Keratin Gold-Nanoparticles in a Nephron-like Microfluidic Chip for Photo-Thermal Therapy Applications. *Mater. Today Adv.*. **2022**, *16*, No. 100286.

https://doi.org/10.1021/acsomega.2c07054
ACS Omega 2023, 8, 4092−4105

(79) Aghanejad, A.; Omidi, Y. Radiolabeled Theranostics: Magnetic and Gold Hybrid Nanoparticles. *Noble Met.-Met. Oxide Hybrid Nanopart.: Fundam. Appl.* **2019**, 535−547.
(80) Shi, L.; Buhler, E.; Boué, F.; Carn, F. How Does the Size of Gold Nanoparticles Depend on Citrate to Gold Ratio in Turkevich Synthesis? Final Answer to a Debated Question. *J. Colloid Interface Sci.* **2017**, *492*, 191−198.
(81) Hameetman, L.; Commandeur, S.; Bavinck, J. N. B.; Wisgerhof, H. C.; de Gruijl, F. R.; Willemze, R.; Mullenders, L.; Tensen, C. P.; Vrieling, H. Molecular Profiling of Cutaneous Squamous Cell Carcinomas and Actinic Keratoses from Organ Transplant Recipients. *BMC Cancer* **2013**, *13*, 58.
(82) Bonamy, C.; Sechet, E.; Amiot, A.; Alam, A.; Mourez, M.; Fraisse, L.; Sansonetti, P. J.; Sperandio, B. Expression of the Human Antimicrobial Peptide β -Defensin-1 Is Repressed by the EGFR-ERK-MYC Axis in Colonic Epithelial Cells. *Sci. Rep.* **2018**, *8*, 18043.
(83) De Chaumont, F.; Dallongeville, S.; Chenouard, N.; Hervé, N.; Pop, S.; Provoost, T.; Meas-Yedid, V.; Pankajakshan, P.; Lecomte, T.; Le Montagner, Y.; Lagache, T.; Dufour, A.; Olivo-Marin, J. C. Icy: An Open Bioimage Informatics Platform for Extended Reproducible Research. *Nat. Methods* **2012**, *9*, 690−696.
(84) Teicher, B. A.; Alvarez, E.; Menon, K.; Esterman, M. A.; Considine, E.; Shih, C.; Faul, M. M. Antiangiogenic effects of a protein kinase Cβ-selective small molecule. *Cancer Chemotherapy and Pharmacology* **2002**, *49*, 69−77.
(85) Kruczynski, A.; Colpaert, F.; Tarayre, J. P.; Mouillard, P.; Fahy, J.; Hill, B. T. Preclinical in vivo antitumor activity of vinflunine, a novel fluorinated Vinca alkaloid. *Cancer Chemotherapy and Pharmacology* **1998**, *41*, 437−447.

https://doi.org/10.1021/acsomega.2c07054
ACS Omega 2023, 8, 4092−4105